Research Square

Preprints are preliminary reports that have not undergone peer review.
They should not be considered conclusive, used to inform clinical practice,
or referenced by the media as validated information.

Laboratory demonstration of electron diffusive shock acceleration via pre-established ambient magnetic turbulence

Bin Qiao

bqiao@pku.edu.cn

Peking University https://orcid.org/0000-0001-7174-5577

X. X. Jin

Peking University https://orcid.org/0009-0005-7677-1631

Zhonghai Zhao

Center for Applied Physics and Technology, HEDPS, and SKLNPT, School of Physics, Peking University, Beijing, China https://orcid.org/0000-0003-2051-1740

Shu-Kai He

Research Center of Laser Fusion

Zhi-meng Zhang

Research Center of Laser Fusion

X. F. Shen

Peking University

Wei Sun

China Institute of Atomic Energy

L. X. Li

Research Center of Laser Fusion, CAEP

Lei Zhu

Center for Applied Physics and Technology, HEDPS, and SKLNPT, School of Physics, Peking University,

Y. L. Xia

Peking University

Dawei Yuan

Key Laboratory of Optical Astronomy, National Astronomical Observatories, Chinese Academy of Sciences

Yu Dai

Institute of Physics

Z. L. Ma

Beijing Normal University

H. H. An

Shanghai Institute of Laser Plasma, CAEP

K. Gu
Shanghai Institute of Optics and Fine Mechanics, CAS

Huiya Liu
Shanghai Institute of Optics and Fine Mechanics

Neng Hua
Shanghai Institute of Optics and Fine Mechanics

Panzheng Zhang
Shanghai Institute of Optics and Fine Mechanics

Zhe Zhang
Institute of Physics https://orcid.org/0000-0001-8076-5094

Jiayong Zhong
Beijing Normal University https://orcid.org/0000-0001-9460-2982

Jianqiang Zhu
National Laboratory on High Power Lasers and Physics

Shaoping Zhu
Institute of Applied Physics and Computational Mathematics

Gang Zhao
Key Laboratory of Optical Astronomy, National Astronomical Observatories, Chinese Academy of Sciences

Jie Zhang
Shanghai Jiao Tong University https://orcid.org/0000-0001-7821-4808

Xiantu He
Physics school

Weimin Zhou
China Academy of Engineering Physics https://orcid.org/0000-0001-5474-7511

Article

Keywords:

Posted Date: November 10th, 2026

DOI: https://doi.org/10.21203/rs.3.rs-11127407/v1

License: This work is licensed under a Creative Commons Attribution 4.0 International License.
Read Full License

Additional Declarations: There is **NO** Competing Interest.

Laboratory demonstration of electron diffusive shock acceleration via pre-established ambient magnetic turbulence

X. X. Jin†,[1] Z. H. Zhao†,[1] S. K. He,[2] Z. M. Zhang,[2] X. F. Shen,[1] W. Sun,[3] L. X. Li,[1,2] Z. Lei,[1,4] Y. L. Xia,[1] D. W. Yuan,[5] Y. Dai,[6] Z. L. Ma,[7] H. H. An,[8] K. Gu,[9] H. Y. Liu,[9] N. Hua,[9] P. Z. Zhang,[9] Z. Zhang,[6] J. Y. Zhong,[7] J. Q. Zhu,[9] S. P. Zhu,[4] G. Zhao,[5] J. Zhang,[10] X. T. He,[4] W. M. Zhou*,[2] and B. Qiao*[1,11]

[1)] *Center for Applied Physics and Technology, HEDPS, and SKLNPT, School of Physics, Peking University, Beijing, China*

[2)] *Science and Technology on Plasma Physics Laboratory, Research Center of Laser Fusion, China Academy of Engineering Physics (CAEP), Mianyang, China*

[3)] *Department of Nuclear physics, China Institute of Atomic Energy, Beijing, China*

[4)] *Institute of Applied Physics and Computational Mathematics, Beijing, China*

[5)] *Key Laboratory of Optical Astronomy, National Astronomical Observatories, Chinese Academy of Sciences, Beijing, China*

[6)] *National Laboratory for Condensed Matter Physics, Institute of Physics, Chinese Academy of Sciences, Beijing, China*

[7)] *Department of Astronomy, Beijing Normal University, Beijing, China*

[8)] *Shanghai Institute of Laser Plasma, CAEP, Shanghai, China*

[9)] *National Laboratory on High Power Laser and Physics, Shanghai Institute of Optics and Fine Mechanics, Chinese Academy of Sciences, Shanghai, China*

[10)] *Key Laboratory for Laser Plasmas (Ministry of Education) and School of Physics and Astronomy, Shanghai Jiao Tong University, Shanghai, China*

[11)] *Frontiers Science Center for Nano-optoelectronic, Peking University, Beijing, China*

(Dated: 17 October 2026)

Diffusive Shock Acceleration (DSA), a well-established first-order Fermi mechanism, is widely recognized as one of the most efficient astrophysical acceleration processes, capable of boosting charged particles to ultra-high energies. For electron DSA to operate, however, seed electrons must exceed an energy threshold to cross the shock front, and strong pitch-angle scattering is required to enable repeated shock crossings. To date, laser-driven experiments at large facilities, including the National Ignition Facility (NIF), have demonstrated only electron pre-acceleration in shock downstream, without achieving full DSA due to the lack of scattering conditions. Here, we report the first laboratory realization of electron DSA, by pre-establishing a fully-developed upstream magnetic turbulence that mimics the space and astrophysical scenarios. We show that turbulent magnetic fluctuations can diffusively scatter low-energy electrons directly into the DSA process, lowering the injection threshold to $\sim$ 210 keV. Consequently, suprathermal electrons are smoothly injected into the full DSA cycle, undergo up to 10 shock crossings and are boosted to relativistic energies ($>$ 500 keV) with a power-law spectrum of index -3. Our findings highlight the crucial role of ambient turbulence in enabling electron DSA, with profound implications for the space and astrophysical shock acceleration and the origin of cosmic rays.

Collisionless shocks are ubiquitous in the Universe. They form when astrophysical flows exceed the characteristic wave speeds of the ambient medium, and dissipate directional kinetic energy through microphysical processes, heating the plasma and accelerating charged particles[1–3]. For instance, the terrestrial bow shock can boost solar wind electrons from thermal to relativistic energies (up to 500 keV)[4]. Broadband synchrotron emission from radio to gamma rays observed in supernova remnants (SNRs) further indicates the presence of ultra-relativistic electrons with energies ranging from GeV to 100 TeV[5–7]. How collisionless shocks accelerate electrons to such high energies remains a fundamental open question in modern astrophysics.

Diffusive shock acceleration (DSA)[8–11], a first-order Fermi mechanism, is widely invoked to explain the high-energy electrons observed in astrophysical settings, as its predicted cutoff energies and spectral slopes agree well with astronomical observations. In DSA, electrons gain energy by repeatedly crossing the collisionless shock front. For electron DSA to operate, however, two key requirements must be met. First, seed electrons must either already possess or be pre-accelerated to an energy above the injection threshold - the minimum energy required to traverse the shock in both directions. In a magnetized collisionless shock, this threshold is governed by the condition that the electron cyclotron radius r_{ce} exceeds

† These authors have contributed to this work equally.
∗ Corresponding author. e-mail: zhouwm@caep.cn, bqiao@pku.edu.cn.

the shock thickness L_s[12,13]. Second, the accelerated electrons must experience sufficiently strong pitch-angle scattering off magnetic irregularities in both upstream and downstream plasmas[1], so that they can return to the shock multiple times and their momentum distribution becomes nearly isotropic in the fluid rest frame.

A number of laboratory experiments at large laser facilities, including the National Ignition Facility, have been carried out to simulate astrophysical collisionless shock acceleration. Two experimental schemes are most commonly investigated. The first involves the collision of laser-driven counter-streaming plasmas[14–16], in which the electromagnetic Weibel instability grows rapidly. This leads to a kinetic, magnetized turbulent plasma with elevated density and temperature at the center and, eventually, to the formation of a double-shock system on both sides. However, owing to the lack of strong turbulent scattering in the upstream, only pre-acceleration without shock crossing - namely, first-order Fermi acceleration occurring solely shock downstream[17] - has been observed. The second scheme employs a laser-driven supersonic outflow impinging on a magnetized ambient plasma[18,19], similar to the earlier magnetic piston concept[20]. In this case, the supersonic outflow strongly compresses the upstream magnetized plasma, forming a shock on a short timescale and accelerating particles via shock surfing acceleration (SSA)[19,21] and shock drift acceleration (SDA)[22,23]. However, because a shock propagating in uniform magnetic field exhibits a pronounced overshoot, particles can hardly gain enough energy within the shock lifetime to freely traverse the shock front. Moreover, even if a few pre-accelerated particles cross the shock and enter the upstream, they quickly escape without pitch-angle scattering. Consequently, full DSA has not yet been achieved.

Recent in-situ observations of planetary bow shocks, such as Earth[4], Saturn[24] and Jupiter[25], have recognized that upstream ambient magnetic fluctuations (foreshock transient, foreshock bubbles and hot flow anomalies, etc.) can significantly lower the injection threshold and enhance shock electron acceleration, with energies reaching the MeV level. For SNRs shock to accelerate cosmic rays up to the knee, observations also show that scattering and diffusion near the shock front has to be dramatically enhanced compared to that in the interstellar medium[26,27]. These imply that the ubiquitous but long overlooked ambient magnetic turbulence in space and astrophysics can promote shock electron acceleration and even the DSA process.

Here we report the first laboratory demonstration of full electron DSA at the Shenguang-II series laser facilities. This milestone is achieved by creating a realistic, astrophysically relevant scenario: a piston-driven collisionless shock propagating into a pre-established, fully developed magnetic turbulence. As we show below, owing to the strong magnetic scattering in this fully developed turbulence, especially in the shock upstream, the electrons over a broad energy range undergo diffusive-convective motion[28,29]. We find that strong turbulent scattering leads to a substantial lowering of the injection threshold ($\sim$ 210 keV in our experiment), and electrons can gain energy by crossing the shock repeatedly over many cycles (up to 10 cycles), thereby reaching relativistic energies ($>$ 500 keV) and producing a power-law spectrum with an index of -3. Our results highlight the overlooked role of ambient magnetic turbulence in enabling electron DSA and provide the first laboratory evidence, with profound implications for the space and astrophysical shock acceleration and the origin of cosmic rays.

RESULTS

Experimental setup

The experiments were conducted at the Shenguang-II (SG-II) and Shenguang-II Upgrade (SG-II-U) laser facilities. Figure 1(a) shows a schematic of the experimental setup, see "Methods" for details. The experimental configuration consists of three parts: one for establishing magnetic turbulence, another for driving a collisionless shock into the turbulence, and the third for diagnostics.

Upstream magnetic turbulence is generated by colliding two laser-driven, counter-streaming plasma flows along the +y and -y directions at the center. The novelty of this scheme lies in the use of perforated CH foils, which enhance the transverse density gradient ∇n_e and temperature gradient ∇T_e of the laser-driven plasma flows. This produces a large number of strong, small-scale toroidal Biermann magnetic structures with field strength $\geq$ 25 T (see Fig. S1 in *Supplementary Materials*). The subsequent interaction of the two counter-streaming flows shears and compresses these magnetic structures, giving rise to fully-developed magnetic turbulence that satisfies the magnetization condition required for shock formation[18,19], similar to the earlier magnetic piston shock concept[20,30].

The collisionless shock is formed by injecting a laser-driven supersonic piston outflow from an ablated CH foil into the pre-established magnetic turbulence (along the +x direction); the shock subsequently accelerates electrons via DSA. By adjusting the relative delay between two groups of laser pulses, we can control the state of the turbulence that interacts with the piston outflow, enabling us to explore the influence of turbulence properties on electron acceleration.

A suite of diagnostics is employed to probe the dynamics of turbulence-mediated collisionless shock formation and the associated electron acceleration. A laser-driven proton beam (propagating in the -z direction) is used to diagnose the turbulent magnetic field and the shock front evolution. The interaction region is also monitored by time-gated and time-integrated X-ray detectors, while the accelerated high-energy electrons are measured by an electron magnetic spectrometer. Additionally, the electron density n_e of the turbulent plasma is diagnosed by

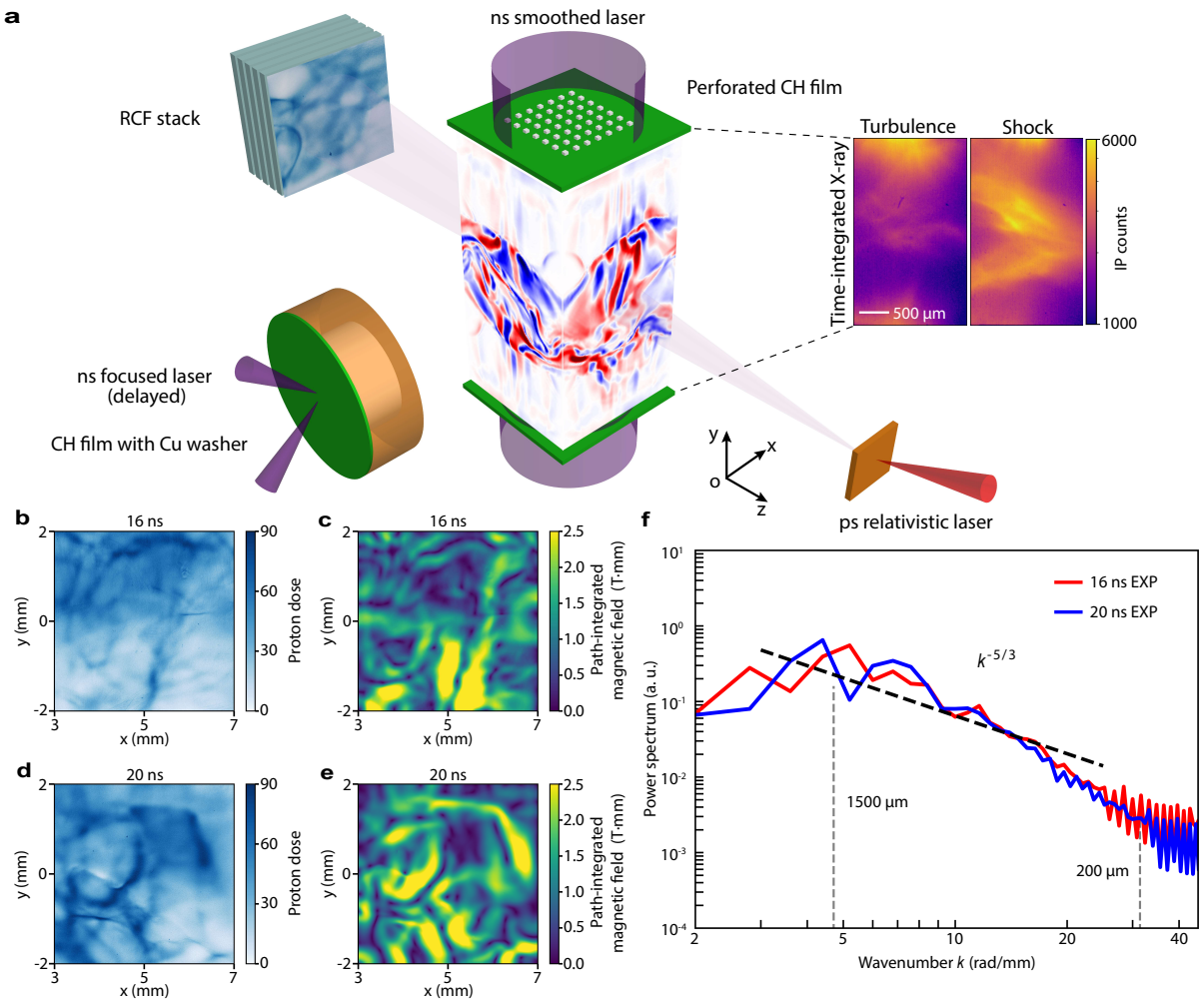


Fig 1. Experimental demonstration of electron DSA at SG-II and SG-II-U laser facilities: setup and characterization of pre-established magnetic turbulence. a, Schematic of the experimental setup, comprising three main components: magnetic-turbulence generation, collisionless-shock driving and evolution, and diagnostics. Turbulence is produced by colliding two counter-streaming plasma flows (along $+y$ and $-y$) generated by ablating through two opposing perforated CH foils (separated by 6 mm) using the first group of CPP-smoothed nanosecond lasers (total energy 1000 J). After a controlled time delay, a second group of Gaussian nanosecond lasers (total energy 1000 J) ablates a 10-μm-thick CH foil located at $x = -5$ mm (mounted in front of a copper washer with a 300-μm-diameter central hole), producing a piston plasma flow that drives the shock into the turbulent region. At the SG-II facility, time-gated and time-integrated X-ray detectors, together with optical diagnostics, monitor turbulence formation and shock evolution. At the SG-II-U facility, a laser-driven proton beam (propagating along $-z$, generated by a 400J picosecond relativistic laser) probes the turbulent magnetic field in the upstream and shock regions. **b,c,** Proton radiography image of upstream magnetic turbulence and the reconstructed path-integrated magnetic field ψ at $t = 16$ ns. **d,e,** same as **b,c,** but at $t = 20$ ns. **f,** Power spectra of the upstream turbulent magnetic field derived from **c** and **e**, fitted with a -5/3 power law. The vertical dashed lines mark the injection and dissipation scales, respectively.

optical diagnostics, and the plasma temperature T_e is measured using a flat-field grating spectrometer.

Characterization of the upstream magnetized turbulence

Figures 1(b) and 1(d) show proton radiography images of the upstream magnetic turbulence at $t = 16$ ns and $t = 20$ ns, respectively, while Figs. 1(c) and 1(e) present the corresponding path-integrated magnetic field ψ, reconstructed using the "PROBLEM" code[31,32]. Both the raw radiographs and the reconstructed fields reveal abundant magnetic fluctuations generated at the colliding center, which exhibit no preferred orientation and are approximately isotropic. Under the assumptions of isotropy and homogeneity[33,34], the magnetic energy spectrum can be recovered as $E_B(k) = kE_\psi(k)/(4\pi^2 l_{\rm path})$, where $E_\psi(k)$ is the normalized 1D spectrum of ψ and $l_{\rm path}$ denotes the proton path length. The resulting spectra $E_B(k)$, shown in Fig. 1(f), display a fully-developed

magnetic turbulence with a -5/3 power law, spanning from an outer scale of ~ 1500 μm down to a dissipation scale of ~ 200 μm. Moreover, the close overlap of the spectra at the two times ($t = 16$ and 20 ns) confirms that the turbulence is in a quasi-steady state, likely sustained by a balance between dynamo amplification and resistive dissipation.

Quantitatively, the in-plane magnetic field strength is estimated as $B_{\rm rms}^2 = (2/\pi l_{\rm path}) \int {\rm d}k\, k\, E_\psi(k)$. Assuming $l_{\rm path} \approx 1$ mm, we obtain $B_{\rm rms} \approx 8.1$ T at $t = 16$ ns and ≈ 7.8 T at $t = 20$ ns. The turbulent magnetic field strengths here are comparable to or slightly weaker than those in previous experiments[19,22]. Those experiments, however, relied on an externally applied uniform magnetic field (about 5–20 T), which is fundamentally different from the self-generated magnetic turbulence here. As shown in Figs. S3 and S4 of the *Supplementary Materials*, the plasma density measured by optical interferometry is $n_e \approx 10^{19}$ cm^{-3} and the electron temperature characterized by the flat-field grating spectrometer is $T_e \approx 74$ eV. Therefore, the magnetization parameter of the turbulence[35] is $\chi_e \equiv \omega_{ce}\tau_e \approx 0.6\,(B/1\ {\rm T})\left(n_{\rm e}/10^{16}\ {\rm cm}^{-3}\right)^{-1}(T_e/1\ {\rm eV})^{3/2} \approx 3.06$, where ω_{ce} is the electron cyclotron frequency and τ_e is the electron collision time. This confirms that the upstream turbulence is fully magnetized and can provide the sufficient pitch-angle scattering required for DSA, as analyzed above.

Shock formation in the pre-established magnetized turbulence

Following the development of upstream turbulence, a supersonic piston outflow, with an estimated velocity $v_{\rm flow} \sim 500$ to 700 km/s, launched from the laser-ablated CH foil, is injected into the turbulent region to drive a collisionless shock. The magnetized condition ($\chi_e \geq 1$) facilitates the rapid formation of this shock[20,30]. Multiple pieces of experimental evidence confirm the formation of a collisionless shock and the influence of the upstream turbulence on its dynamics.

Firstly, the emission images recorded by a time-gated X-ray detector in Figs. **2**(a) and **2**(b) reveal the morphologies of the shocked downstream plasma, as the emission intensity scales as $I_{\rm X-ray} \propto Z^3 n_i^2 T_e^{1/2}$ (assuming Bremsstrahlung dominates[30]). We see that an early ($t =$ 20 ns) bow-shaped structure evolves into a broadened and fragmented structure at a later time $t = 22$ ns, indicating that the shock continuously sweeps through the upstream turbulent plasma. Time evolution of the vertically averaged X-ray profiles is shown in Fig. **2**(c), from which the entire shock formation process can be clearly observed: the downstream plasma densities ($n_i \propto I_{\rm X-ray}^{1/2}$) undergo a transition from piling-up to dissipation, accompanied by a maximum 9-fold enhancement in emission (comparing the blue and yellow line peaks), corresponding to a maximum density compression ratio $R = n_{\rm down}/n_{\rm up} \approx 3$. This estimate is also consistent with the optical interferometry image shown in Fig. S3 of the *Supplementary Materials*, and together they indicate the formation of a moderately strong shock. From temporal evolution of the emission peak, the shock velocity is measured to be $v_{\rm sh} \approx 350 \pm 50$ km/s, and we list the relevant parameters characterizing the turbulence and the collisionless shock in Table I. It is particularly noteworthy that the ion–ion mean free path $\lambda_{ii} \approx 6.2$ cm is much larger than the characteristic system scale $L_{\rm sys} \approx 0.4$ cm, confirming that the shock is indeed collisionless.

Secondly, the proton radiography images of the shock formation region at $t = 18$ and 22 ns in Figs. **2**(d) and **2**(e) reveal the magnetic field compressions and discontinuities at the shock front. The distortion of the shock front, marked by the black arrow in **2**(d), clearly demonstrates the role of upstream turbulence in modulating the shock front shape as the turbulent magnetic field is compressed and amplified. The left part of Fig. **2**(e) shows that at a later time the shocked downstream region becomes broadened and more chaotic, where the ripple structures trailing the shock front indicate the amplified turbulent field downstream (see the region marked by the red dashed line). The reconstructed path-integrated magnetic field ψ at $t = 22$ ns is shown in the right half of **2**(e); the value at the shock front, $\psi \geq 2.0$ T $\cdot$ mm, is larger than the upstream turbulent $\psi_{\rm rms} \sim 1.5$ T $\cdot$ mm [Figs. **1**(c) and **1**(e)], revealing considerable magnetic field amplification. To further characterize the spatial properties of nonstationary structures in the shocked downstream, we extract lineouts of the proton dose and the reconstructed field along the red-dashed bow-shaped line from top to bottom in Fig. **2**(f). Both lineouts exhibit multiple peaks and valleys with spatial scales about $300 \sim 400$ μm, which fall within the inertial range of the original upstream turbulence [see Fig. **1**(f)]. Therefore, turbulence not only provides the magnetization conditions necessary for shock formation, but also generates abundant turbulent fluctuations of comparable scale across the shock. Such fields enable electrons to be repeatedly reflected back and forth at the shock and to enter the diffusive acceleration regime, thereby preventing the premature escape that would otherwise be caused by sharp variations in scattering conditions.

2D3V PIC simulations for reproducing the turbulence-mediated collisionless shock

The experimental features of the turbulence-mediated collisionless shock are reproduced and further elaborated using 2D3V particle-in-cell (PIC) simulations. As detailed in "Methods", the measured power spectra of the turbulent magnetic fields [Fig. **1**(f)] are used to initialize the turbulent field in the PIC simulation.

The spatial distributions of the in-plane magnetic field $B_{xy} = \sqrt{B_x^2 + B_y^2}$ (normalized by the upstream field strength B_{xy0}) at $t = 19$ and 22 ns are shown in Figs. **3**(a)

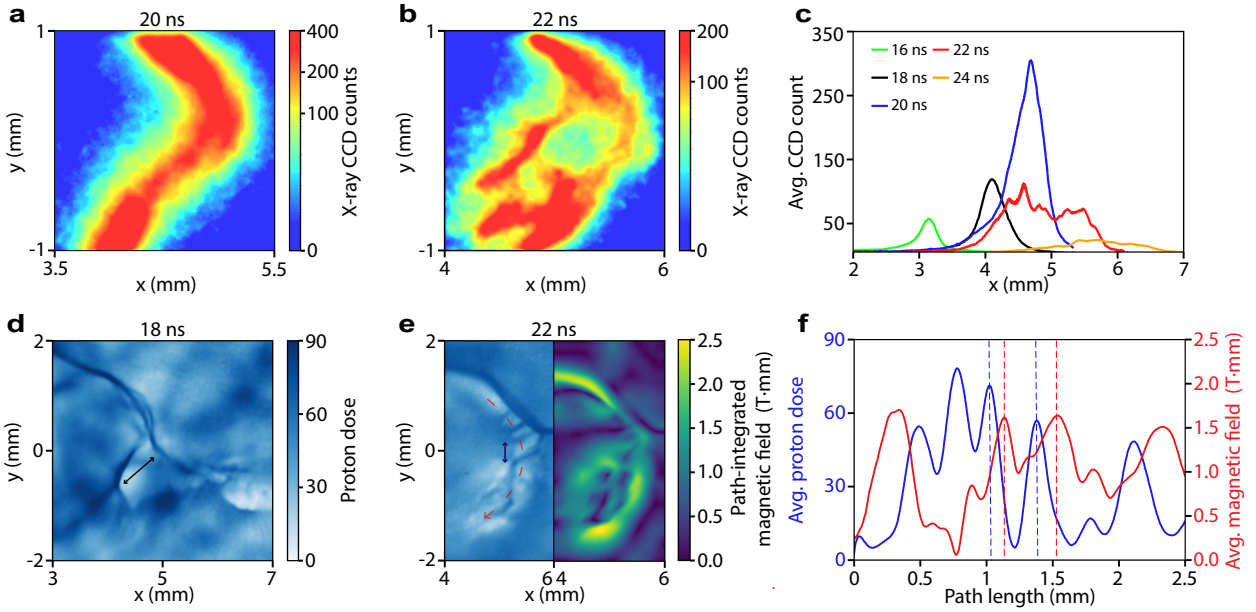


Fig 2. X-ray emission and proton radiography of collisionless shock formation in pre-established magnetized turbulence. **a,b,** X-ray self-emission images (logarithmic color scale) of the shock region at $t = 20$ and 22 ns. **c,** Time evolution of the vertically averaged X-ray emission profiles from $t = 16$ to 24 ns. **d,e,** Proton radiography images of the shock region at $t = 18$ and 22 ns; the reconstructed path-integrated magnetic field ψ is also shown (overlaid in **e**). **f,** Lineouts of the proton dose (blue) and the reconstructed field (red) along the red-dashed bow-shaped line from top to bottom in panel (e). The vertical dashed lines mark the spatial separations between multiple peaks, which are approximately $300 \sim 400$ μm.

and **3**(d), respectively. The vertically averaged x-axis profiles of B_x (green) and B_y (blue), together with the electron density profiles of the piston flow (red-dashed) and the ambient turbulence (red-solid), are plotted in Figs. **3**(b) and **3**(e). Consistent with the experimental observations in Fig. **2**, Fig. **3**(a) shows that as the supersonic piston flow is injected into magnetic turbulence, electron density piles up and turbulent field is amplified, yielding a maximum density compression ratio $R \approx 3$, matching the experiment. Moreover, the electron densities of the piston and the turbulence in **3**(b) are clearly separated, confirming that the shock is driven predominantly by the upstream turbulent magnetic field rather than by fields generated through the Weibel instability from interpenetrating plasma flows.

At $t = 22$ ns, the rich small-scale field structures developed in the downstream region [**3**(d)] are in close agreement with the radiograph in Fig. **2**(e), confirming the intricate interaction between the collisionless shock and the magnetic turbulence. Furthermore, the shock front detaches completely from the piston front, and the shocked plasma broadens to millimeter scales [**3**(e)], where the conventional Foot–Ramp–Overshoot shock structure is no longer discernible[36] and the field is dominated by multi-scale meandering structures. Finally, the fully kinetic nature of the PIC simulation allows us to identify in Fig. **3**(c) the characteristic phase space signature of upstream $CH^{3.5+}$ ions reflected by the collisionless shock[37].

In DSA, strong pitch-angle scattering of magnetic turbulence drives the electron momentum distribution $f(t, x, p)$ to evolve via diffusive-convective motion in the fluid rest frame[28,29]. The evolution is governed by the Parker transport equation[10,38] $\frac{\partial f}{\partial t} = -u\frac{\partial f}{\partial x} + \frac{\partial}{\partial x}\left[\overline{D}(x,p)\frac{\partial f}{\partial x}\right] + \frac{p}{3}\frac{du}{dx}\frac{\partial f}{\partial p}$, where the three right-hand terms represent convection, diffusion, and adiabatic compression, respectively. The quasi-steady diffusion coefficient $\overline{D}(x, p)$ depends on the magnetic field irregularities (both fluctuating and mean components) in turbulences. Using the turbulent magnetic field from our PIC simulations [Figs. **3**(a) and **3**(d)], we perform a large number of small-scale test-particle simulations[27,39]. The local $\overline{D}(x, p)$ is obtained by statistical averaging over a small spatial domain and taking the asymptotic steady-state value. To sample $\overline{D}(x, p)$ at different positions [e.g., the 14 blue and 14 red points in Fig. **3**(f)], we have performed 28 test-particle simulations for electrons of 210 keV, each in a small domain of size 0.125 mm. Details are provided in Section III of *Supplementary Materials*, which includes a specific example for the green triangle data point in Fig. **3**(f), see Fig. S5. Note that, because proton radiography yields only the 2D topology B_{xy} (with no B_z information) and has limited spatial resolution, $\overline{D}_x(t)$ cannot be accurately derived from the experimental data. Nevertheless, a crude estimate of the transport characteristics is provided in Fig. S6 of *Supplementary Materials*.

Figure **3**(f) shows that the diffusion coefficient $\overline{D}_x$ decreases markedly from the upstream region (e.g., the blue and red diamond points) to the shock front (yellow circle and green triangle points) at both $t = 19$ and

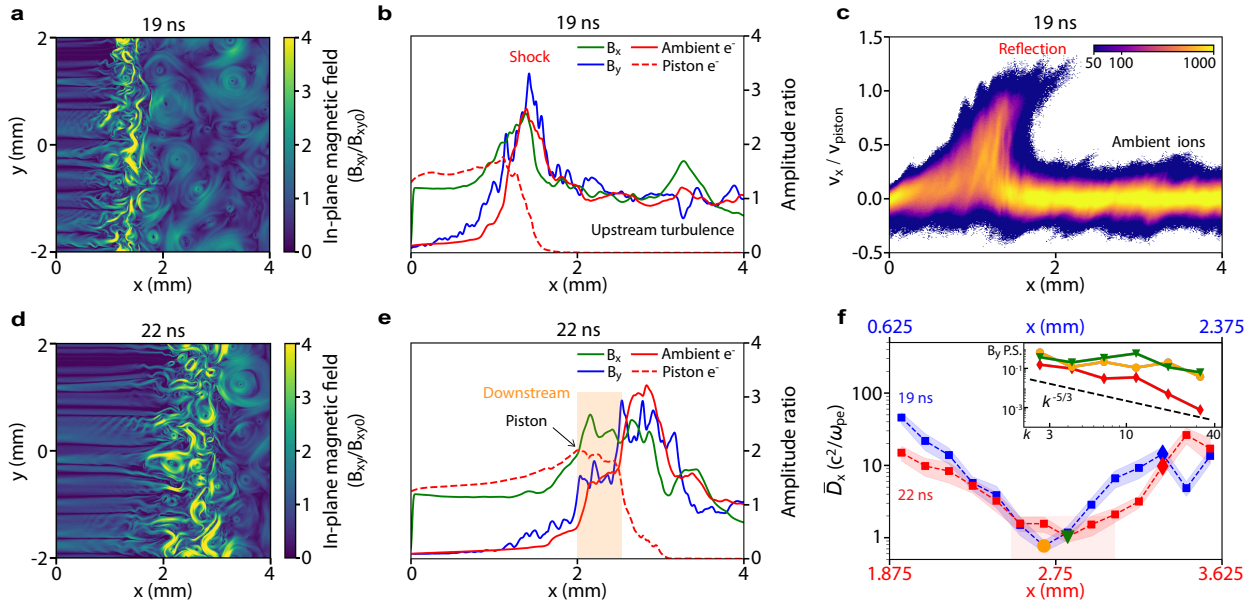


Fig 3. Results of 2D3V PIC simulations reproducing the turbulence-mediated collisionless shock. a, Spatial distributions of the in-plane magnetic field $B_{xy} = \sqrt{B_x^2 + B_y^2}$ (normalized by the upstream field strength B_{xy0}) at $t = 19$ ns. **b,** Vertically averaged x-axis profiles of B_x (green) and B_y (blue), together with electron density profiles of the piston flow (red-dashed) and the ambient turbulence (red-solid) at $t = 19$ ns. **c,** Phase space distribution in $(x–v_x)$ plane of the ambient $CH^{3.5+}$ ions. **d,** same as **a** but at a later time $t = 22$ ns. **e,** same as **b** but at $t = 22$ ns. **f,** Local diffusion coefficient $\overline{D}_x$ at various x-positions near the shock region, obtained from a series of supplementary test-particle simulations. The inset shows the magnetic power spectra corresponding to the symbols with the same color; the black-dashed line indicates a -5/3 power-law.

22 ns. This reduction is attributed to amplification of the magnetic field strength and development of small-scale turbulent field structures near the shock front, as evidenced by their corresponding magnetic power spectra (insets). For instance, comparing the red diamond value ($\overline{D}_x \approx 9.76\ c^2/\omega_{pe}$) and the green triangle value ($\overline{D}_x \approx 1.02\ c^2/\omega_{pe}$) yields a reduction factor of more than 9. This is substantially larger than that expected for a collisionless shock in a uniform magnetic field, where the reduction factor should be only 3 according to the maximum density compression ratio (or magnetic field amplification ratio) $R \approx 3$. Thus, the critical role of the pre-established upstream turbulence is clearly identified.

More importantly, at $t = 22$ ns, the reduction of $\overline{D}_x$ down to values below 2.0 c^2/ω_{pe} extends over a broad spatial region of 0.6 mm in the turbulent upstream and downstream regions near the shock front, further confirming that diffusion governs electron transport and acceleration. This strong suppression of $\overline{D}_x$ implies a significant decrease in the characteristic DSA acceleration time, since $t_{ac}(x) \sim \overline{D}_x(x)/v_{sh}^2$ [27]. With the experimental shock velocity $v_{sh} \approx 400$ km/s, the characteristic acceleration time is estimated as only ~ 0.46 ns (for $\overline{D}_x \approx 2.0\ c^2/\omega_{pe}$). Given that the collisionless shock persists for about 8 ns in the experiment, electrons undergo DSA for more than 10 cycles, thereby enabling them to reach relativistic energies of approximately 500 keV[26].

Full DSA of electrons

The measured time-integrated electron energy spectra for different experimental cases are plotted in Fig. 4(a). For the case with only upstream turbulence (no piston flow injection), the yellow spectrum decays rapidly and shows a rather low cut-off energy, as no collisionless shock forms and thus no effective acceleration occurs. For the case with only a supersonic piston outflow (without pre-establishing magnetic turbulence), the black line exhibits a suprathermal tail with a cut-off energy of $E_c \approx 350$ keV, indicating the absence of electron DSA. For the fiducial case, in which a supersonic piston flow is injected into fully-developed magnetic turbulence (with a delay of $\Delta t = 10$ ns after the turbulence-driving lasers, see "Methods"), the red line displays a clear DSA power-law spectrum with an index of about -3 and a cut-off extending into the relativistic regime ($E_c > 500$ keV), confirming that full DSA is achieved. The number of accelerated high-energy electrons is also substantially enhanced. This power-law spectrum is reproduced by our 2D-PIC simulations. In Fig. 4(b), instead of the time-integrated spectrum, the temporal evolution of the transient electron spectra is shown. Through DSA, the spectrum evolves from a thermal distribution to an E^{-3} power-law within about 6 ns (from 16 to 22 ns), in good agreement with the experimental measurement.

To investigate the influence of magnetic-turbulence properties on electron DSA, experiments with various

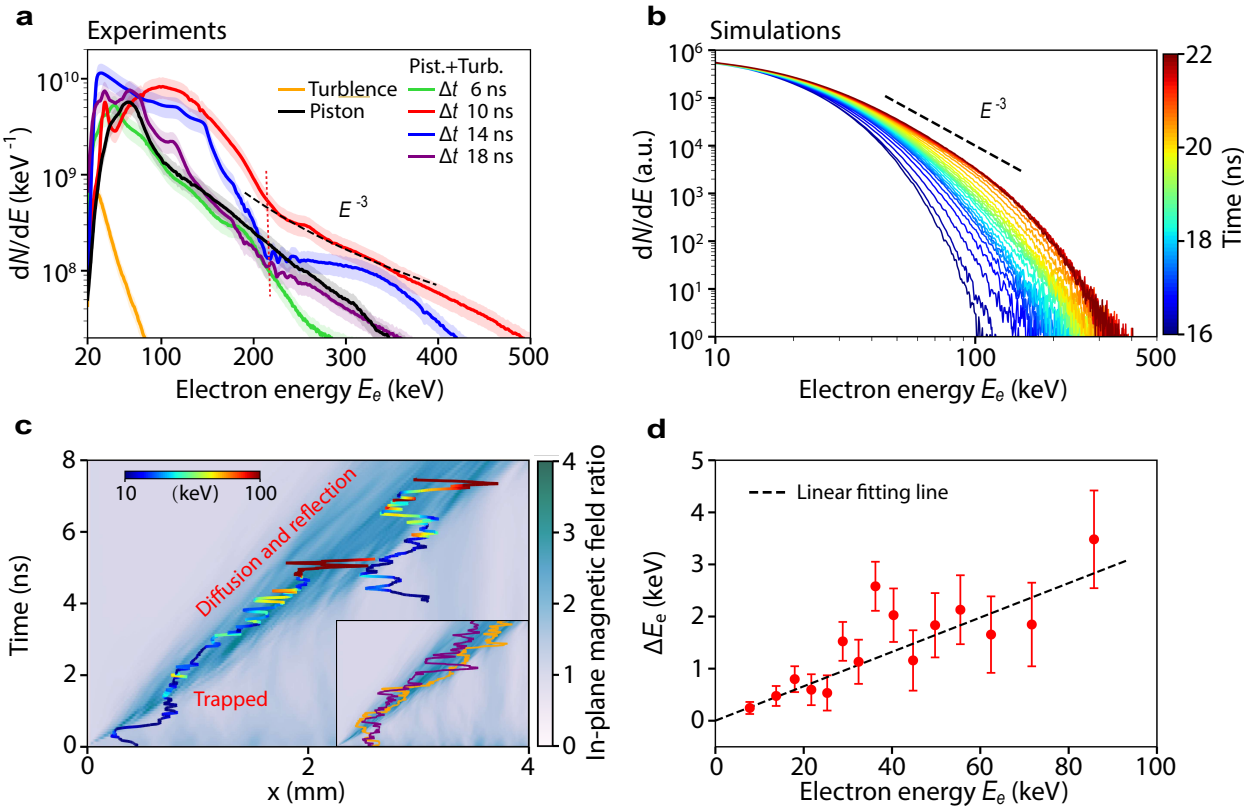


Fig 4. Electron energy spectra measured in the experiments and obtained from PIC simulations. **a,** Measured time-integrated electron energy spectra (along $+x$ direction) for different experimental configurations: turbulence only (yellow), piston only (black), and piston-turbulence interactions with different delays between the piston driving and the turbulence driving laser of $\Delta t = 6$ (green), 10 (red, fiducial shot), 14 (blue), and 18 ns (purple). **b,** Time evolution of the transient electron energy spectra obtained from the PIC simulation corresponding to the fiducial shot. **c,** Trajectories and corresponding energy evolutions of representative DSA electrons overlaid on the in-plane magnetic field strength. The inset shows the trajectories of two additional DSA electrons. **d,** Statistical variation of the electron energy gain ΔE_e as a function of the electron energy E_e per DSA cycle. The dashed line represents a linear fit, and the error bar indicates one standard deviation.

time delays Δt are carried out. When the piston flow is injected either too early [$\Delta t = 6$ ns, green line in Fig. 4(a)] before the turbulence is fully developed, or too late [$\Delta t = 18$ ns, purple line] after the turbulence has dissipated, no effective DSA is observed. For an intermediate delay $\Delta t = 14$ ns (blue line), although a well-defined power law is not obtained, a significant increase in the number of electrons above 210 keV is evident.

Another important feature in the measured electron spectra is the break point at $E_{\rm break} \sim 210$ keV [marked by the vertical dashed line in Fig. 4(a)], where the spectral index changes from nearly suprathermal to -3. This indicates that only electrons with energies above 210 keV undergo DSA; in other words, the injection threshold for electron DSA in our experiment is $E_{\rm inj} \sim 210$ keV. This value is much smaller than the classical threshold of about 790 keV derived from the condition $r_{ce} \geq L_s$. In a turbulence-mediated collisionless shock, however, the injection criterion is expressed in terms of the turbulence diffusion length $l_{\rm diff} \geq L_s$. Assuming that the dissipation scale k_*^{-1} of upstream turbulence sets the minimum effective scale for the diffusion approximation[28], the injection threshold can be derived as $p_{\rm inj}/m_e V_{\rm A} \geq (m_i/m_e)(k_* d_i)^{-1}$, where $p_{\rm inj}$, $V_{\rm A}$ and d_i are the electron injection momentum, Alfvén speed and ion inertia length, respectively[28,29]. Substituting the measured values $B_{\rm rms} \approx 8$ T, $d_i \approx 98$ μm, $(k_*)^{-1} \approx 200$ μm yields $E_{\rm inj} \approx 190$ keV, which agrees well with the observed break point of 210 keV in Fig. 4(a).

The detailed electron diffusion acceleration process is clearly illustrated by tracing typical DSA electron trajectories in PIC simulations, shown in Fig. 4(c). The trajectories reveal that electrons are initially trapped and pre-accelerated at the shock front, and subsequently gain energy through repeated shock crossings - a hallmark of DSA[40]. The energy gain per upstream-downstream-upstream cycle is shown in Fig. 4(d), yielding $\Delta E_e/E_e \sim v_{\rm flow}/v_e \sim 0.033$, where $v_e \sim 0.7c$ is taken as the typical electron velocity. This value is consistent with the prediction of the first-order Fermi acceleration. Both the experimental measurements and theoretical estimates support the conclusion that these electrons enter the DSA regime,

facilitated by pitch-angle scattering off turbulence.

DISCUSSION

In summary, we have presented the first laboratory demonstration of electron diffusive shock acceleration, one of the most efficient astrophysical acceleration processes, achieved at the SG-II series laser facilities. By creating an astrophysically relevant scenario in which a piston-driven collisionless shock propagates into a pre-established, fully-developed magnetic turbulence, we have realized full DSA of electrons. The critical roles of the pre-established turbulent environment have been identified: providing strong pitch-angle scattering that substantially lowers the electron injection threshold, enabling multiple shock crossings, and facilitating momentum isotropization. Such effects were absent in previous experiments, which relied either on colliding counter-streaming plasmas[14–16] or on driving supersonic outflow into uniformly magnetized ambient plasmas[18,19]. Our measurements show that electrons above 210 keV smoothly enter the full DSA cycle, undergo more than 10 shock crossings, and are accelerated to relativistic energies ($>$ 500 keV) with a power-law spectrum of index -3, in excellent agreement with first-order Fermi acceleration predictions.

Our findings provide new insights into the injection and acceleration mechanisms operating in space and astrophysical environments, and could be applied to understand recent observations. For example, the broadband waves in the foreshock transients of Earth's bow shock can facilitate electron scattering, lowering the injection threshold to 1-5 keV and allowing multiple shock crossings, which result in reinforced acceleration and a canonical spectral index of -2[4]. Similarly, the quasi-parallel portion of Saturn's bow shock, characterized by large-amplitude magnetic fluctuations ($\delta B/B_0 \sim 10$), can efficiently accelerate electrons to MeV energies[24]. Interstellar turbulence with $\delta B/B_0 \sim 1$ also has the potential to promote electron DSA in SNRs shock by enhancing spatial diffusion, provided that the dissipation scales approach the ion inertial scale[41]. Our results provide the first experimental evidence that, in addition to conventional shock parameters such as the Alfvénic Mach number and the magnetic obliquity, the upstream turbulence plays a pivotal role in governing shock acceleration and its efficiency, which could also provide guidance for future observations, such as the Magnetospheric Multiscale mission and Juno.

Moreover, we have established a robust laboratory platform for studying shock acceleration. In the present experiment, only kilojoule-level laser energy was used, and a moderate-Mach-number collisionless shock was formed, yet it was sufficient to drive electron DSA. Looking ahead, the use of higher-energy lasers (e.g., 100 kJ) could generate stronger shocks and larger-scale upstream turbulence, where enhanced spatial diffusion may initiate DSA of protons, opening a new frontier for laboratory astrophysics.

METHODS

Details of experimental setup

As shown in the above schematic Fig. 1(a), the experiments were conducted at the SG-II and SG-II-U laser facilities of the Shanghai Institute of Optics and Fine Mechanics, Chinese Academy of Sciences. The SG-II-U facility additionally provides a picosecond relativistic laser beam that enables proton radiography.

In the SG-II experiment, eight nanosecond laser beams at the wavelength of 351 nm are used, each delivering approximately 250 J of energy in a 2 ns square pulse. These beams are split into two independent groups of four, with an adjustable delay between them. The first group drives two counter-streaming plasma flows along the +y and -y directions by ablating through two opposing perforated CH foils with a separation of 6 mm. Each foil is irradiated by two nanosecond laser beams with a 300 μm spot size, shaped by continuous phase plates (CPPs), and a total energy of 500 J. The perforated foil is patterned with a 7×7 array of 60 μm-diameter holes spaced by 120 μm in the x–z plane, and has a thickness of 5 μm with 3% Cl doping. The subsequent interaction of the two counter-streaming flows at the center ($y = 0$) results in the formation of fully developed magnetic turbulence.

After specific delay times of 6, 10, 14 and 18 ns, the second group of four nanosecond laser beams, focused to 150 μm Gaussian spots with a total energy of 1000 J, is used to drive the piston plasma flow along the x-direction. This piston flow is generated by ablation through a 10 μm-thick CH foil (also doped with 3% Cl) located 5 mm away at $x = -5$ mm, which is mounted in front of a copper washer with a 300 μm-diameter central hole. Reference shots with only the piston flow or only turbulent flows are also performed for comparison.

On the SG-II facility, time-gated and time-integrated X-ray detectors together with optical diagnostics, are used to monitor the formation of the magnetic turbulence and the subsequent shock. The plasma electron density n_e is diagnosed by interferometry, and the plasma temperature T_e is measured with a flat-field grating spectrometer. The accelerated high-energy electrons are characterized by an electron magnetic spectrometer covering an energy range of 20–600 keV, placed 20 cm away at $x = 20$ cm. The detailed setup of these diagnostics is shown in Fig. S2 of the Supplementary Information.

In the SG-II-U experiment, four nanosecond laser beams are used, where, by contrast, each beam delivers 500 J of energy in a 2 ns square pulse. To match the laser conditions of the SG-II experiment, each perforated foil is ablated by a single CPP-smoothed nanosecond laser beam with the same 500 J energy, and the piston flow is driven by two focused nanosecond laser beams with the same total energy of 1000 J. All target parameters are kept identical. A unique capability of the SG-II-U facility is the picosecond relativistic laser beam, which delivers approximately 400 J in a pulse duration of $\sim$1.5 ps, focused to a spot size of $\sim$ 30 μm. This beam irradiates a 10 μm-thick gold foil to generate protons via target normal sheath acceleration. An additional 10 μm-thick aluminum foil is placed 0.8 mm in front of the target to mitigate the preheating effects from the nanosecond laser ablation. The resulting proton beam, propagating along the -z direction, is used for proton radiography of the turbulent magnetic fields and the shock front evolution.

RMHD simulations performed using FLASH code

The radiation-magnetohydrodynamic (RMHD) simulations in this work are carried out by using the code "FLASH"[42], which has been extended to include many high energy density physics modeling capabilities including laser energy deposition, multi-temperature ($T_e \neq T_i \neq T_{rad}$), anisotropic electron thermal conductivity, and radiation transport, etc. We have also further augmented the code with self-consistent magnetic field modeling, incorporating the Biermann battery, Nernst convection, resistive diffusion, Righi-Leduc effects and so on, that is the reason why we called it "RMHD".

Three-dimensional (3D) RMHD simulations are carried out to investigate the generation of Biermann magnetic fields from laser ablated planar and perforated CH foil targets, with initial conditions matching those of the experiments. The simulation domain is $2 \times 8 \times 2$ mm^3 in the (x, y, z) directions. Two opposing perforated CH foils, each 2 mm in diameter, are attached to a copper washer (1 mm inner diameter, 0.25 mm thickness) and are placed separately at $y = +3$ mm and $y = -3$ mm. The CH foil density is $\rho_{\rm CH} = 1.02$ g/cm^3 and the thickness is 5 μm, consistent with the experiments. Each foil is irradiated by two nanosecond laser beams with a 300 μm CPP-smoothed spot size and delivering a total energy of 500 J. The copper density is $\rho_{\rm Cu} = 8.92$ g/cm^3. The equation of state (EOS) and opacity of CH and Cu come from the code "BADGER"[43] and "IONMIX"[44], respectively. All initial temperatures are set to be uniform at room temperature $T_0 \approx 290$ K. Fully implicit electron thermal conductivity is adopted, and the flux limiter is selected as a typical 0.06.

PIC simulations using WarpX code

The kinetic particle-in-cell (PIC) simulations are performed using the WarpX code[45] in a 2D3V configuration (two spatial dimensions in the (x, y) plane and three velocity components). To model the turbulent magnetic fields observed in the experiment, we initialized all three components of the magnetic field by inverting the magnetic power spectrum [Fig. 1(f)] inferred from proton radiography above the dissipation scale. The resulting field is generated using a matrix operator derived from a Gaussian random field, which enforces the divergence-free condition in 2D Fourier space $\vec{k} \cdot \mathcal{F}[\vec{B}(r)] = 0$.

In the simulations, the ion species of the CH plasma is assumed to be $CH^{3.5+}$, and the ion-to-electron mass ratio is set to the realistic value $m_i/m_e = 11934$. The corresponding ion and electron densities are initialized based on the measured experimental value $n_e = 10^{19}$ cm^{-3}, assuming quasi-neutrality. In order to simulate the full DSA evolution and acceleration process over the several-nanosecond timescale, we increase the initial electron temperature from the measured value $T_e = 74$ eV to 7.4 keV, i.e., a scaling factor of $f_{T_e} = 100$, which corresponds to a thermal velocity scaling factor $f_{v_{te}} = 10$. Consequently, 100 ps in the PIC simulations corresponds to approximately 1 ns in the experiments, giving a temporal scaling factor $f_t = 10$. The scaled simulation domain spans 12×4 mm^2 in the (x, y) directions, from $x = -6$ mm till $x = 6$ mm. It consists of 12288×4096 cells, yielding a spatial resolution of $0.0098\, d_i$, where d_i is the ion inertial length. We use 32 macro-particles per species per cell with third-order shape functions. Open boundaries are applied along x, while periodic boundaries are used along y. The right half of the domain ($x \in [0, 6]$ mm) is initialized with the turbulent magnetic field and a uniform ambient plasma density, while the left half ($x \in [-6, 0]$ mm) is initialized with a uniform piston plasma flow of the same density and with a velocity of $0.023c$ (scaled by the same factor of 10, i.e. 10 times higher than the experimental value of 700 km/s).

Because it is difficult to obtain time-integrated escaping electron energy spectra directly from 2D3V PIC simulations, we define a moving window that follows the upstream region, extending from the shock front $x_{\rm sh}$ to $x_{\rm sh} + 2$ mm. The transient electron energy spectra are then calculated within this window as a function of time. This approach excludes the primary piston-induced heating and allows us to study the temporal evolution of the electron spectrum from a thermal distribution to non-thermal features.

To trace the typical DSA electron trajectories, we additionally initialize 10^5 electrons with unique tracers, randomly placed in the right half of simulation domain. Corresponding tracer ions are also injected to maintain initial charge neutrality.

DATA AVAILABILITY

All data that support the findings of this study are available from the corresponding author upon reasonable request.

CODE AVAILABILITY

The FLASH code is publicly available at https://flash.rochester.edu, the WarpX code is publicly available at https://github.com/BLAST-WarpX/warpx, and the PROBLEM code is publicly available at https://github.com/flash-center/PROBLEM.

REFERENCES

[1] Treumann, R. A. Fundamentals of collisionless shocks for astrophysical application, 1. Non-relativistic shocks. *Astron. Astrophys. Rev.* **17**, 409–435 (2009).

[2] Bykov, A. M. & Treumann, R. A. Fundamentals of collisionless shocks for astrophysical application, 2. Relativistic shocks. *Astron. Astrophys. Rev.* **19**, 42 (2011).

[3] Marcowith, A. et al. The microphysics of collisionless shock waves. *Reports Prog. Phys.* **79**, 046901 (2016).

[4] Raptis, S. et al. Revealing an unexpectedly low electron injection threshold via reinforced shock acceleration. *Nat. Commun.* **16**, 488 (2025).

[5] Dubner, G. & Giacani, E. Radio emission from supernova remnants. *Astron. Astrophys. Rev.* **23**, 3 (2015).

[6] Vink, J. Supernova remnants: the X-ray perspective. *Astron. Astrophys. Rev.* **20**, 49 (2011).

[7] Aharonian, F. et al. Primary particle acceleration above 100 TeV in the shell-type supernova remnant RX J1713.7-3946 with deep HESS observations. *Astron. Astrophys.* **464**, 235–243 (2007).

[8] Bell, A. R. The acceleration of cosmic rays in shock fronts – I. *Mon. Not. R. Astron. Soc.* **182**, 147–156 (1978).

[9] Blandford, R. D. & Ostriker, J. P. Particle acceleration by astrophysical shocks. *Astrophys. J.* **221**, L29–L32 (1978).

[10] Drury, L. O'C. An introduction to the theory of diffusive shock acceleration of energetic particles in tenuous plasmas. *Rep. Prog. Phys.* **46**, 973–1027 (1983).

[11] Blandford, R. & Eichler, D. Particle acceleration at astrophysical shocks: A theory of cosmic ray origin. *Phys. Rep.* **154**, 1–75 (1987).

[12] Malkov, M. A. & Volk, H. J. Theory of ion injection at shocks. *Astron. Astrophys.* **300**, 605–626 (1995).

[13] Malkov, M. A. & Volk, H. J. Diffusive ion acceleration at shocks: The problem of injection. *Adv. Space Res.* **21**, 551–554 (1998).

[14] Huntington, C. M. et al. Observation of magnetic field generation via the Weibel instability in interpenetrating plasma flows. *Nat. Phys.* **11**, 173–176 (2015).

[15] Fiuza, F. et al. Electron acceleration in laboratory-produced turbulent collisionless shocks. *Nat. Phys.* **16**, 916–920 (2020).

[16] Yuan, D. et al. Electron stochastic acceleration in laboratory-produced kinetic turbulent plasmas. *Nat. Commun.* **15**, 5897 (2024).

[17] Grassi, A. et al. Electron injection via modified diffusive shock acceleration in high-Mach-number collisionless shocks. *Astrophys. J. Lett.* **958**, L32 (2023).

[18] Schaeffer, D. B. et al. Generation and evolution of high-Mach-number laser-driven magnetized collisionless shocks in the laboratory. *Phys. Rev. Lett.* **119**, 025001 (2017).

[19] Yao, W. et al. Laboratory evidence for proton energization by collisionless shock surfing. *Nat. Phys.* **17**, 1177–1182 (2021).

[20]Paul, J. W. M. et al. Experimental observations on the structure of collisionless shock waves in a magnetized plasma. *Nature* **208**, 133–135 (1965).
[21]Yao, W. et al. Detailed characterization of a laboratory magnetized supercritical collisionless shock and of the associated proton energization. *Matter Radiat. Extremes* **7**, 014402 (2022).
[22]Tang, H.-b. et al. Laboratory observation of ion drift acceleration via reflection off laser-produced magnetized collisionless shocks. *Sci. Adv.* **11**, eadn3320 (2025).
[23]Zhang, T. et al. Asymmetric ion acceleration in laser-produced magnetized collisionless shocks. *Matter Radiat. Extremes* **11**, 027402 (2026).
[24]Masters, A. et al. Electron acceleration to relativistic energies at a strong quasi-parallel shock wave. *Nat. Phys.* **9**, 164–167 (2013).
[25]Raptis, S. et al. Relativistic electron acceleration at the bow shock of Jupiter and beyond. *Nature* 654, 47–51 (2026).
[26]Blasi, P. & Amato, E. Diffusive propagation of cosmic rays from supernova remnants in the Galaxy. I: spectrum and chemical composition. *J. Cosmol. Astropart. Phys.* **2012**, 010 (2012).
[27]Caprioli, D. & Spitkovsky, A. Simulations of ion acceleration at non-relativistic shocks. III. Particle diffusion. *Astrophys. J.* **794**, 47 (2014).
[28]Amano, T. et al. Nonthermal electron acceleration at collisionless quasi-perpendicular shocks. *Rev. Mod. Plasma Phys.* **6**, 29 (2022).
[29]Amano, T. & Hoshino, M. Theory of electron injection at oblique shock of finite thickness. *Astrophys. J.* **927**, 132 (2022).
[30]Li, C. K. et al. Collisionless shocks driven by supersonic plasma flows with self-generated magnetic fields. *Phys. Rev. Lett.* **123**, 055002 (2019).
[31]Bott, A. F. A. et al. Proton imaging of stochastic magnetic fields. *J. Plasma Phys.* **83**, 905830614 (2017).
[32]Zhao, Z. et al. Laboratory evidence of Weibel magnetogenesis driven by temperature gradient using three-dimensional synchronous proton radiography. *Sci. Adv.* **10**, eadk5229 (2024).
[33]Graziani, C. et al. Inferring morphology and strength of magnetic fields from proton radiographs. *Rev. Sci. Instrum.* **88**, 123507 (2017).
[34]Tzeferacos, P. et al. Laboratory evidence of dynamo amplification of magnetic fields in a turbulent plasma. *Nat. Commun.* **9**, 591 (2018).
[35]Gregori, G., Reville, B. & Miniati, F. The generation and amplification of intergalactic magnetic fields in analogue laboratory experiments with high power lasers. *Phys. Rep.* **601**, 1–34 (2015).
[36]Gedalin, M. Rankine–Hugoniot relations in turbulent shocks. *Front. Phys.* **11**, 1325995 (2023).
[37]Schaeffer, D. B. et al. Kinetic simulations of piston-driven collisionless shock formation in magnetized laboratory plasmas. *Phys. Plasmas* **27**, 042901 (2020).
[38]Guo, F., Giacalone, J. & Zhao, L. Shock Propagation and Associated Particle Acceleration in the Presence of Ambient Solar-Wind Turbulence. *Front. Astron. Space Sci.* **8**, 644354 (2021).
[39]Gupta, S., Caprioli, D. & Spitkovsky, A. Speed-dependent threshold for electron injection into diffusive shock acceleration. *Astrophys. J. Lett.* **994**, L34 (2025).
[40]Xu, R., Spitkovsky, A. & Caprioli, D. Electron acceleration in one-dimensional nonrelativistic quasi-perpendicular collisionless shocks. *Astrophys. J. Lett.* **897**, L41 (2020)
[41]Lee, K. H. & Lee, L. C. Interstellar turbulence spectrum from in situ observations of Voyager 1. *Nat. Astron.* **3**, 154–159 (2019).
[42]Fryxell, B. et al. FLASH: an adaptive mesh hydrodynamics code for modeling astrophysical thermonuclear flashes. *Astrophys. J. Suppl. Ser.* **131**, 273–334 (2000).
[43]Heltemes, T. A. & Moses, G. A. BADGER v1.0: A Fortran equation of state library. *Comput. Phys. Commun.* **183**, 2629–2646 (2012).
[44]Macfarlane, J. J. IONMIX-A CODE FOR COMPUTING THE EQUATION OF STATE AND RADIATIVE PROPERTIES OF LTE AND NON-LTE PLASMAS. *Comput. Phys. Commun.* **56**, 259–278 (1989).
[45]Fedeli, L. et al. Pushing the frontier in the design of laser-based electron accelerators with groundbreaking mesh-refined particle-in-cell simulations on exascale-class supercomputers. Paper presented at the SC22: The International Conference for High Performance Computing, Networking, Storage and Analysis(SC), Dallas, Texas, 13–18 November 2022.

ACKNOWLEDGEMENTS

This work is supported by the Science Challenge Project, No. TZ2025012; the National Key R&D Program of China, Nos. 2022YFA1603200, 2022YFA1603201, and 2022YFA1603203; the National Natural Science Foundation of China, grants Nos. 12135001, 11921006, 11825502, and 12305267; the Strategic Priority Research Program of the Chinese Academy of Sciences, grant No. XDA25050900. B.Q. acknowledges support from the National Natural Science Funds for Distinguished Young Scholars, grant No. 11825502. The simulations were carried out on the Tianhe-2 supercomputer at the National Supercomputer Center in Guangzhou.

AUTHOR CONTRIBUTIONS

B.Q. and W.M.Z. proposed and were in charge of the research campaign as principal investigators. X.X.J., Z.H.Z., X.F.S., L.X.L., Z.L., Y.L.X., S.P.Z., G.Z., J.Z., X.T.H. carried the simulations, the data analysis. X.X.J., Z.H.Z, S.K.H., Z.M.Z., X.F.S., W.S., D.W.Y., Y.D., Z.L.M., H.H.A., K.G., H.Y.L, N.H., P.Z.Z., Z.Z., J.Y.Z., J.Q.Z. carried out the experiments. B.Q., X.X.J. and Z.H.Z. wrote the paper. B.Q. and W.M.Z. contribute to theoretical interpretations of the results.

COMPETING INTERESTS

The authors declare no competing interests.

ADDITIONAL INFORMATION

Correspondence and requests for materials should be addressed to B.Q. or W.M.Z..

TABLE I. Derived parameters for turbulent upstream and collisionless shock

Parameters	Definition	Value
Magnetization parameter $\omega_{ce}\tau_e$	$6{\times}10^{15} B {n_e}^{-1} {T_e}^{3/2}$	$\omega_{ce}\tau_e \approx 3.06 > 1$ [a]
Ion-ion mean-free-path λ_{ii}	$6.7{\times}10^{9} A^4 {v_r}^4/(Z^4(2A)^2 n_i \ln\Lambda)$	6.2 cm
Collisionality	$L_{\rm sys}/\lambda_{ii}$	0.065
Mach number M_s	$v_{\rm sh}/c_s$	5.3
Alfvénic Mach number M_A	$v_{\rm sh}/v_A$	9.7
Turbulence-mediated injection threshold	$k_* r_{ce} \sim 1$	$E_{\rm inj} \sim 190$ keV

[a] Derived parameters describing the experimental platform are based on the flow conditions, including: upstream electron density $n_e = Zn_i \approx 10^{19}$ cm^{-3}, $A = 6.5$, $Z = 3.5$, upstream magnetic field $B \approx 8$ T, turbulence dissipation scale ${k_*}^{-1} \approx 200$ μm, $v_r = v_{\rm flow} \approx 700$ km/s, $v_{\rm sh} \approx 400$ km/s, and plasma temperature $T_e \approx 74$ eV.

Supplementary Files

This is a list of supplementary files associated with this preprint. Click to download.

- SupplementaryInformation.pdf